

Research Paper

Melting temperature of iron under the Earth's inner core condition from deep machine learning

Fulun Wu^a, Shunqing Wu^a, Cai-Zhuang Wang^b, Kai-Ming Ho^b, Renata M. Wentzcovitch^{c,d,e}, Yang Sun^{a,*}^a Department of Physics, Xiamen University, Xiamen 361005, China^b Department of Physics, Iowa State University, Ames, IA 50011, USA^c Department of Applied Physics and Applied Mathematics, Columbia University, New York, NY 10027, USA^d Department of Earth and Environmental Sciences, Columbia University, New York, NY 10027, USA^e Lamont–Doherty Earth Observatory, Columbia University, Palisades, NY 10964, USA

ARTICLE INFO

Article history:

Received 7 April 2024

Revised 20 June 2024

Accepted 4 September 2024

Available online 12 September 2024

Handling Editor: K. Szilas

Keywords:

Inner core boundary

Melting temperature

Machine learning

Solid-liquid coexistence

Free energy calculation

Molecular dynamics simulation

ABSTRACT

Constraining the melting temperature of iron under Earth's inner core conditions is crucial for understanding core dynamics and planetary evolution. Here, we develop a deep potential (DP) model for iron that explicitly incorporates electronic entropy contributions governing thermodynamics under Earth's core conditions. Extensive benchmarking demonstrates the DP's high fidelity across relevant iron phases and extreme pressure and temperature conditions. Through thermodynamic integration and direct solid–liquid coexistence simulations, the DP predicts melting temperatures for iron at the inner core boundary, consistent with previous *ab initio* results. This resolves the previous discrepancy of iron's melting temperature at ICB between the DP model and *ab initio* calculation and suggests the crucial contribution of electronic entropy. Our work provides insights into machine learning melting behavior of iron under core conditions and provides the basis for future development of binary or ternary DP models for iron and other elements in the core.

© 2024 China University of Geosciences (Beijing) and Peking University. Published by Elsevier B.V. on behalf of China University of Geosciences (Beijing). This is an open access article under the CC BY-NC-ND license (<http://creativecommons.org/licenses/by-nc-nd/4.0/>).

1. Introduction

The Earth's core plays a critical role in the thermal and compositional evolution of our planet (Nimmo, 2015; Voosen, 2022). The core contains a solid inner core and a liquid outer, which form a solid–liquid coexistence (SLC) at the inner-core boundary (ICB). Both inner and outer cores are primarily made of iron. It's generally believed iron has a hexagonal close-packed (hcp) phase under inner core conditions (Steinle-Neumann et al., 2001; Hirose et al., 2013), while the body-centered cubic (bcc) phase is also suggested to be relevant for the inner core structure (Vočadlo et al., 2008; Belonoshko et al., 2017; Sun et al., 2024). The melting temperature of iron under Earth's core conditions is a key factor for constraining the temperature of the Earth's center, understanding the core's property and studying the solidification process of the inner core (Laio et al., 2000; Alfè et al., 2002a; Alfè, 2009; Gubbins et al., 2011; Anzellini et al., 2013; Li et al., 2020; Turneare et al., 2020; Hou et al., 2021; He et al., 2022; Kraus et al., 2022; Zhang

and Lin, 2022; Wu and Wang, 2022; Liu et al., 2023; Wilson et al., 2023; Zhang et al., 2023a). Despite its importance, the melting temperature of iron in the inner core was not well constrained. Experimental measurements reported different results ranging from 4850 K to 7600 K due to the difficulties in generating extreme conditions and detecting melts (Fischer, 2016). The recent experiments still have uncertainties of ~500 K for the melting temperature measurement at ICB conditions (Li et al., 2020; Kraus et al., 2022).

Another avenue for exploring the extreme pressure–temperature conditions within Earth's interiors is through computer simulations. These simulations offer a valuable alternative to experimental methods, allowing us to probe the properties of iron under core conditions. Depending on the modeling approach used to describe interatomic interactions, these simulations can be categorized as classical or *ab initio* simulations. Classical molecular dynamics (CMD) simulations employ semi-empirical potentials to represent interatomic interactions. Due to the efficiency of these potentials, CMD can simulate atomic structures at large length scales and over significant time scales, such as millions of atoms over nanoseconds. This allows the direct simulation of solid–liquid equilibria at the ICB conditions so that the melting temperature

* Corresponding author.

E-mail address: yangsun@xmu.edu.cn (Y. Sun).

can be directly extracted (Morris et al., 1994). However, the limitation of CMD is that the simulation results highly depend on the accuracy of the employed semi-empirical potential. Different semi-empirical potential simulations have yielded varying melting temperatures for iron at inner core pressures. For instance, in 2000, Laio et al. (2000) suggested a low iron melting point of ~ 5400 K at ICB, while Belonoshko et al. (2000) reported a high melting temperature of ~ 7100 K for hcp at the ICB. Recently, Davies et al. (2019) reported a melting temperature of 6215 K for hcp Fe at 323 GPa, a pressure close to the ICB, while Sun et al. (2022) obtained 5860 K at the same pressure with another semi-empirical potential. Using a different potential, Belonoshko et al. (2021, 2022a) showed the hcp melting temperature of ~ 6400 K at ICB.

Compared to CMD, the *ab initio* molecular dynamics (AIMD) simulations provide more accurate descriptions of the interatomic interaction based on the first-principles electronic structure calculations with density functional theory (DFT) (Kohn, 1999). However, due to the time and length scale limitations of DFT, direct SLC simulations with AIMD are usually computationally expensive and involve large uncertainty (Bouchet et al., 2013). The lowest uncertainty of iron's melting temperature from *ab initio* SLC was achieved by Alfè (2009) using 980 atoms for hcp phases, resulting in 6200 ± 150 K. The free energy approach is more widely used to measure the melting temperature from the AIMD simulations. It is based on the explicit calculation of the Gibbs free energy difference between solid and liquid phases, usually involving thermodynamic integration (TI). TI provides the free energy difference between the target and reference systems for which the absolute free energy is known *a priori*. Depending on the different reference systems, the technical details of TI can be different. For instance, Alfè et al. (2002b) employed an inverse-power-law system as the liquid reference and harmonic crystal as the solid reference and obtained the melting temperature of hcp iron as 6350 ± 300 K at 330 GPa (6290 K at 323 GPa). Alfè et al. (2002b) also used a semi-empirical embedded-atom model as the reference states for solid and liquid iron and obtained the melting temperature as 6250 ± 100 K at 323 GPa. Sun et al. (2018) used the Weeks-Chandler-Andersen gas model for the liquid reference in the TI and a phonon quasiparticle method to compute the free energy of the hcp phase, which resulted in a melting temperature of 6170 ± 200 K at 330 GPa. Recently, Sun et al. (2023) also demonstrated that the embedded-atom model is an efficient reference state for TI calculations and reported a melting temperature of 6357 ± 45 K at 323 GPa. González-Cataldo and Militzer (2023) employed a classical pair potential in TI and reported a melting temperature of 6523 ± 8 K at 330 GPa. Therefore, the melting temperatures of the hcp phase from *ab initio* TI calculations are most consistent within the uncertainties, except that González-Cataldo and Militzer's results are ~ 200 K higher than others. It has been frequently suggested that the number of valence electrons considered in the DFT calculation can significantly affect the measurement of melting temperature for iron under inner-core conditions (González-Cataldo and Militzer, 2023; Sun et al., 2018, 2023). Because at high pressures, Fe's semi-core electron orbitals of neighboring atoms can overlap and contribute to metallic bonding, affecting the melting properties (Alfè et al., 2002b). It typically requires 16 valence electrons, i.e., $3s^2 3p^6 3d^6 4s^2$, to address the high-pressure effect and converge free energy calculations. The melting temperature can be underestimated with $3d^6 4s^2$ electrons (Sun et al., 2018, 2023) while overestimated with $3p^6 3d^6 4s^2$ electrons (González-Cataldo and Militzer, 2023).

As the pure AIMD simulations remain a heavy burden for computer resources, interatomic potentials developed with machine learning techniques have significantly extended the timescale and length scale of simulation and maintained the *ab initio* accu-

racy (Behler, 2021; Deringer et al., 2021; Unke et al., 2021; Wen et al., 2022). The algorithms, such as Neural Network Potential (NNP) (Behler and Parrinello, 2007), Gaussian Approximation Potential (GAP) (Bartók et al., 2010), on-the-fly Machine Learning Force Field (MLFF) (Jinnouchi et al., 2019), and Deep Potential (DP) (Zhang et al., 2018b) can incorporate large amounts of *ab initio* data to construct direct mappings from atomic structures to forces and energies, thus saving significant amounts of computational time required for *ab initio* calculation. The melting temperatures of iron under inner core conditions have also recently been studied using machine learning potentials. In particular, Zhang et al. (2020b) developed a GAP model for iron and reported a melting temperature of 6253 ± 170 K at 330 GPa, consistent with previous *ab initio* results. However, Yuan and Steinle-Neumann (2023) developed a DP model and reported iron's melting temperature as $7000\text{--}7100$ K with an uncertainty of 35 K at 330 GPa. The value predicted by the DP model is significantly higher than those obtained from CMD and AIMD calculations, falling within the range of $6000\text{--}6400$ K, as summarized above. So far, no explanation has been provided for the large discrepancy. In recent studies, DP models have shown high accuracy in simulating complex minerals in the Earth's interior, as demonstrated by a few groups in the study of bridgmanite (Luo et al., 2021; Yang et al., 2022; Deng et al., 2023; Wan et al., 2024), davemaoite (Wu et al., 2024), FeSiO melts (Zhang et al., 2022; Tang et al., 2023), and δ -AlOOH (Luo et al., 2024), etc. Its poor performance in estimating iron's melting temperature under inner core conditions is alarming, given that a few studies on elemental partitioning rely on the DP method (Yuan and Steinle-Neumann, 2023).

This work aims to develop an accurate DP model and determine melting temperatures for iron phases under inner core pressures with free energy calculations and the SLC method. We will include factors relevant to iron's melting temperature under core conditions. By comparing the present DP model and Yuan's DP model, we try to identify key factors leading to the discrepancy with AIMD results and provide new insight into iron melting behavior under Earth's core conditions.

The paper is organized as follows: Section 2 discusses computational methods used for the DP model development and simulation details. Section 3 provides benchmarks of the present DP model and calculations of melting temperature, and discusses the origin of the discrepancy in Yuan's DP model. At the end, Section 4 concludes the paper.

2. Research methods

2.1. Deep-learning potential with electronic entropy contribution

We developed the DP model for iron under inner core conditions based on the smooth edition descriptor *se_e2_a* proposed by Zhang et al. (2018a, 2018b). This descriptor integrates both angular and radial information of atomic configurations to encode the local environment of iron within the cutoff radius. The descriptors $\{D_1, D_2, \dots, D_i\}$ were used to calculate the free energy via a deep neural network. For an electron-ion system the free energy F is defined as the Mermin free energy (Mermin, 1965; Wentzcovitch et al., 1992),

$$F = E + T_{\text{el}} S_{\text{el}} \quad (1)$$

where T_{el} is the electronic temperature, E is the self-consistent energy from the Kohn-Sham formalism with orbital occupancies f_{kn} as

$$f_{\text{kn}}(T_{\text{el}}) = \left(1 + \exp \frac{\hbar(E_{\text{kn}} - E_f)}{k_B T_{\text{el}}} \right)^{-1} \quad (2)$$

where E_{kn} is the one-electron energy of an orbital with wavenumber \mathbf{k} and band index n , and E_f is the Fermi energy. S_{el} is the electronic entropy, defined by

$$S_{el}(f_{kn}, T_{el}) = -k_B \sum_{\mathbf{k}, n} [(1 - f_{kn}) \ln(1 - f_{kn}) + f_{kn} \ln f_{kn}] \quad (3)$$

The electronic entropy contribution plays a key role in determining the free energy of metals, particularly important for iron under high pressure and temperature conditions (Zhuang et al., 2021). Fig. 1 shows the training scheme to incorporate the electronic entropy contribution in the neural network model, which results in an electronic temperature-dependent DP model. This method has been previously applied to warm dense matter across a wide range of temperatures, accurately describing the thermodynamic properties over a broad range of electron temperatures and ion densities (Zhang et al., 2020a). As shown in Fig. 1, the local environment surrounding each atom i and electronic temperature T_{el} are input parameters. The total free energy F is obtained by summing up the contributions from all atoms, $F = \sum_{i=1}^N F_i$. To preserve physical symmetry, the relative coordinates of atoms were mapped onto generalized coordinates, $\hat{x}_{ji} = \frac{s(r_{ji})x_{ji}}{r_{ji}}$, using a continuous and differentiable scalar weighting function, $s(r_{ji})$. The neighbor atom cutoff radius was set to 6.0 Å. Our embedding and fitting neural networks had three hidden layers with {25, 50, 100} and {240, 240, 240} neurons, respectively. We randomly initialized the neural network and trained it for 1,000,000 steps using the Adam stochastic gradient descent method (Kingma and Ba, 2014). We set the learning rate to decrease exponentially, with the decay step and decay rate being 5000 and 0.96, respectively. The loss function was defined as a combination of the energy prefactor p_e , force prefactor p_f , and virial prefactor p_ξ (Zhang et al., 2018a) as

$$L(p_e, p_f, p_\xi) = \frac{p_e}{N} \Delta A^2 + \frac{p_f}{3N} \sum_i |\Delta F_i|^2 + \frac{p_\xi}{9N} \|\Delta \Xi\|^2 \quad (4)$$

where the root mean square errors in energy, force, and virial were represented by ΔA , ΔF and $\Delta \Xi$, respectively. We started with the energy prefactor p_e at 0.2 and gradually increased to 1, while the virial prefactor p_ξ started at 0.01 and gradually increased to 0.1. The force prefactor p_f decreased from 1000 to 1 to achieve the desired accuracy in force prediction.

2.2. Density functional theory calculations

DFT calculations were conducted to prepare training data of iron using the Vienna *Ab-initio* Simulation Package (VASP) (Kresse and Hafner, 1993; Kresse and Furthmüller, 1996), which implements the projector-augmented wave (PAW) methodology (Blöchl, 1994; Perdew et al., 1996). The exchange–correlation functional was treated with the generalized gradient approximation (GGA) (Perdew et al., 1996) in the form of the Perdew–Burke–Ernzerhof (PBE) formula. PAW potential with 16 valence electrons ($3s^2 3p^6 3d^7 4s^1$) was used for iron. The plane wave energy cutoff was set to 750 eV. The Brillouin zone was sampled using a Monkhorst-Pack scheme with a \mathbf{k} -point mesh of $2 \times 2 \times 2$. This setting has been shown to achieve the high accuracy necessary for iron under Earth's core conditions (Sun et al., 2018, 2023). The electronic entropy in DFT calculations is described by the Mermin functional (Mermin, 1965; Wentzcovitch et al., 1992), with the electronic temperature T_{el} kept the same as the ionic temperature. The DFT calculations were performed with 288 atoms for hcp, 250 atoms for bcc, and 250 for liquid.

2.3. Thermodynamic integration

To calculate the free energies with sufficient time and length scales, the TI scheme developed in Sun et al. (2023) was employed, which provides a transformation of the Hamiltonian from a classical reference system to the DP system. We used the classical embedded-atom model developed in Sun et al. (2022) as the refer-

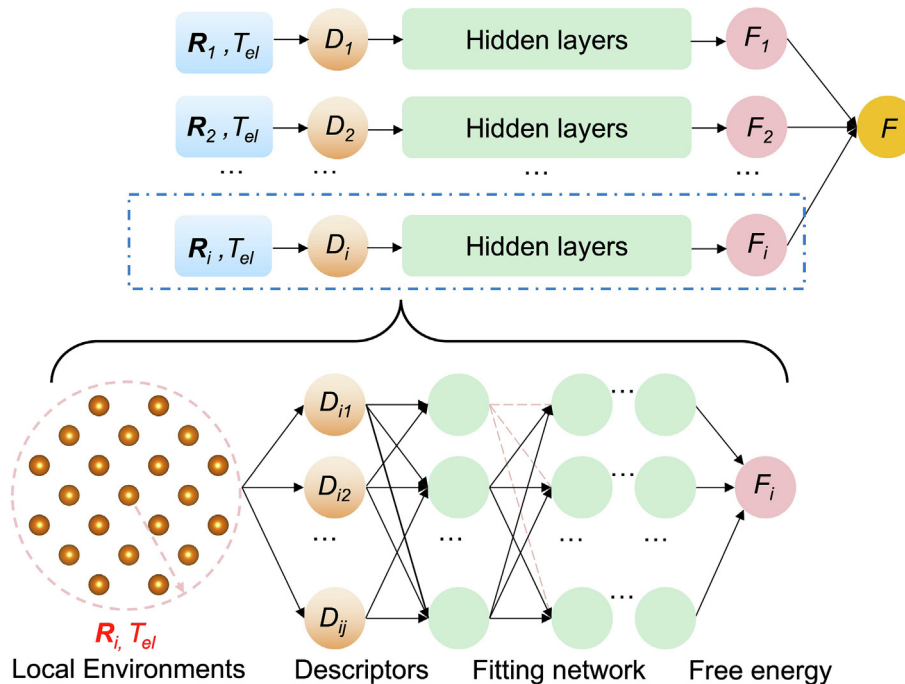


Fig. 1. The scheme to calculate the atomic free energy of iron from their local environment using a neural network. The atomic local environment $\{\mathbf{R}_1, \mathbf{R}_2, \dots, \mathbf{R}_i\}$ and electronic temperature (T_{el}) are used as input parameters.

ence state, where the classical free energy difference between liquid and solid was computed, denoted as $\Delta G_c^{L-S}(T)$. The transformation from classical free energy $\Delta G_c^{L-S}(T)$ to DP free energy $\Delta G_{DP}^{L-S}(T)$ can be obtained by considering the contribution $f_{pV}(T)$ from the equation of state (EoS) difference between DP and classical systems, and the Helmholtz free energy contribution $f_{\pi}(T)$ computed by the TI between the liquid and solid phases as

$$\Delta G_{DP}^{L-S}(T) = \Delta G_c^{L-S}(T) + f_{pV}(T) + f_{\pi}(T) \quad (5)$$

$$f_{pV}(T) = \left[P(V_A^L - V_A^S) - P(V_C^L - V_C^S) \right] - \int_{V_C^L}^{V_{DP}^L} P_C^L(V) dV + \int_{V_C^S}^{V_{DP}^S} P_C^S(V) dV \quad (6)$$

$$f_{\pi}(T) = \int_0^1 \langle U_{DP}^L - U_C^L \rangle_{\lambda, NVT} d\lambda - \int_0^1 \langle U_{DP}^S - U_C^S \rangle_{\lambda, NVT} d\lambda \quad (7)$$

where V_{DP}^L (or V_{DP}^S) and V_C^L (or V_C^S) are the equilibrium volumes of the liquid (or solid) at pressure P for DP and classical systems, respectively. $P_C^L(V)$ and $P_C^S(V)$ represent the equation of states of the liquid and solid for the classical system, respectively. U_{DP}^L (or U_{DP}^S) and U_C^L (or U_C^S) are the internal energies of the liquid (or solid) for DP and classical systems, respectively. The ensemble average of the internal energy over configurations $\langle \cdot \rangle_{\lambda, NVT}$ was sampled in the canonical ensemble with the mixed force field $U = (1 - \lambda)U_{DP} + \lambda U_C$. The subscript NVT represents the constant conditions of (V_{DP}^L, T) and (V_{DP}^S, T) in the liquid and solid simulations, respectively. The TI was performed with 2000 atoms for hcp, bcc, and liquid phases.

2.4. Solid-liquid coexisting method

The solid-liquid coexisting method was also employed to determine the melting point of iron (Morris et al., 1994). To prepare the two-phase configurations with a solid-liquid interface, an iron slab with 15,552 atoms was first equilibrated at a target temperature. Then, half of the atoms were fixed while the other half were heated until melting occurred. The liquid part was subsequently cooled to the target temperature and the entire slab was subjected to the target temperature, allowing one phase to grow at the expense of the other over time. The melting temperature was identified as the temperature at which the liquid population either increased above or decreased below the test value. The polyhedral template matching algorithm (Larsen et al., 2016) as employed for efficient local structure analysis. The populations of hcp-like and liquid-like atoms were computed based on the root mean square deviation between the atomic clusters and templates from the perfect crystals (Sun et al., 2016; Wen et al., 2017).

3. Results and discussion

3.1. Benchmarks of the deep potentials

The configurations obtained from the *ab initio* data span various pressure and temperature ranges, covering 323–360 GPa and 6300–6700 K, as depicted in Supplementary data (Fig. S1). To evaluate the accuracy of the T_{el} -dependent DP model, we examined the root mean square errors (RMSEs) of the energies, atomic forces, and pressures for iron and compared them with the corresponding density functional theory (DFT) calculations, as shown in Fig. 2a–c. We found an excellent agreement between the results of the T_{el} -dependent DP model and DFT. The RMSEs were approximately 4.6 meV/atom for energies, 0.32 eV/Å for forces, and 0.47 GPa for pressures. Fig. 2a also revealed a wide distribution of energies,

suggesting a sufficient exploration of complex configuration spaces on the potential energy surface. We compared the computational cost with DFT, DP, and EAM across various system sizes. As shown in Supplementary data (Fig. S1), the DP model demonstrates significant efficiency advantages, particularly in large-scale simulations where traditional DFT methods become computationally prohibitive.

We further investigated the RMSEs of the DP when the electronic entropy was not specifically included in the training procedure, and compared them with the results obtained from DFT calculations. Fig. 2d–f clearly illustrates substantial discrepancies in energy and pressure between the DP and DFT outcomes. The discrepancies can be attributed to the inconsistent electronic entropy at different temperatures. This highlights the significance of incorporating the electronic entropy contribution in the training process for iron under inner core conditions to correctly describe the free energy. The force was not affected by the electronic entropies. By inspecting Yuan's (2023) training dataset, we found the AIMD simulations in Yuan and Steinle-Neumann (2023) were performed with a fixed electronic temperature $T_{el} = 6000$ K for different ionic temperatures. In contrast, we adjust the electronic temperature to match the ionic temperatures during the AIMD simulations, providing a more realistic representation of electronic entropy effects. Therefore, Yuan and Steinle-Neumann's (2023) training dataset and DP model might fail to describe the electronic entropy contribution correctly, which can contribute to the discrepancies in the melting temperatures predicted by our model and Yuan and Steinle-Neumann's (2023) DP model.

The DP model is further validated by comparing the equation of state (EOS) of iron phases. Fig. 3 shows the EOS of bcc, hcp, and liquid iron obtained from DP simulations agree well with recent DFT calculations and experiments (Martorell et al., 2015; Kuwayama et al., 2020; Belonoshko et al., 2022b). This further suggests the present DP model can well describe all bcc, hcp and liquid phases under core conditions.

3.2. Melting temperatures

We first use the free energy calculation to compute the melting temperature for the present DP model. Based on the TI method, we compute the Gibbs free energy difference between solid and liquid, ΔG^{L-S} , under various pressure and temperature conditions. Fig. 4 shows the Gibbs free energy difference as a function of temperature at 360 GPa. A negative value of ΔG^{L-S} implies that the liquid phase is more thermodynamically stable compared to the solid phase, while $\Delta G^{L-S}(T) = 0$ corresponds to the melting temperature $T = T_m$. In Fig. 4a, the DP-based simulations resulted in melting temperatures of 6656 K for hcp and 6480 K for bcc at 360 GPa. Compared to previous AIMD simulations (Sun et al., 2023), ΔG^{L-S} curves of both hcp and bcc only show a difference of 3–5 meV/atom at the melting points. However, this small energy difference yields a melting temperature ~ 40 K lower. This suggests the melting temperature is very sensitive to the accuracy of free energy calculations. Nevertheless, the present DP model provides a satisfactory description of the free energy compared to previous AIMD data. In Fig. 4b, our T_{el} -DP model provides a very different melting curve compared to the DP model generated by Yuan and Steinle-Neumann (2023) with a difference of more than 600 K.

Because the melting temperatures in Yuan and Steinle-Neumann (2023) were computed by SLC simulations, we also computed the hcp melting temperature by the SLC simulations to examine whether different melting temperature calculation methods could introduce errors. Fig. 5 shows the change of hcp populations in a series of SLC simulations at different temperatures at 330 GPa. The increase of the hcp atom number indicates the simu-

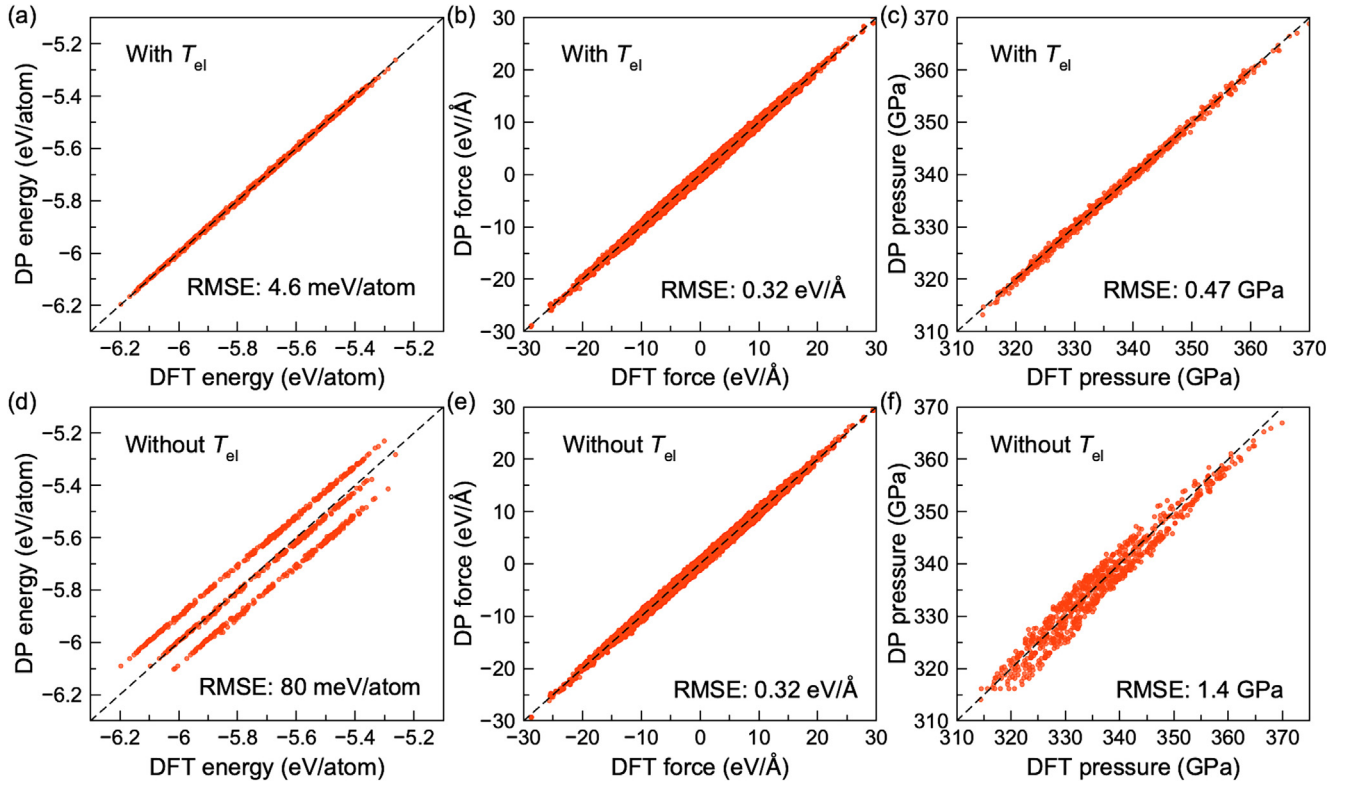


Fig. 2. Comparisons of (a) energies, (b) atomic forces, and (c) pressures between DFT and the T_{el} -dependent DP model. (d–f) denote the results between DFT and DP trained without the electronic entropy contribution. The black dashed lines are guides for perfect matches.

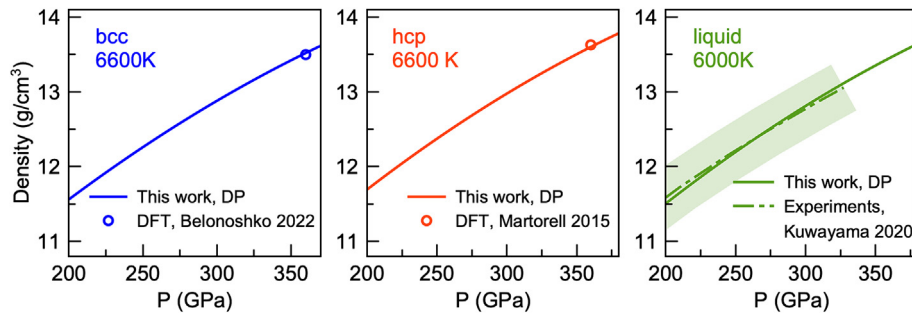


Fig. 3. Equation of state of bcc, hcp, and liquid iron between DP and DFT (Martorell et al., 2015; Belonoshko et al., 2022b) or experimental results (Kuwayama et al., 2020). The shadow in the liquid EoS curve is the experimental uncertainty.

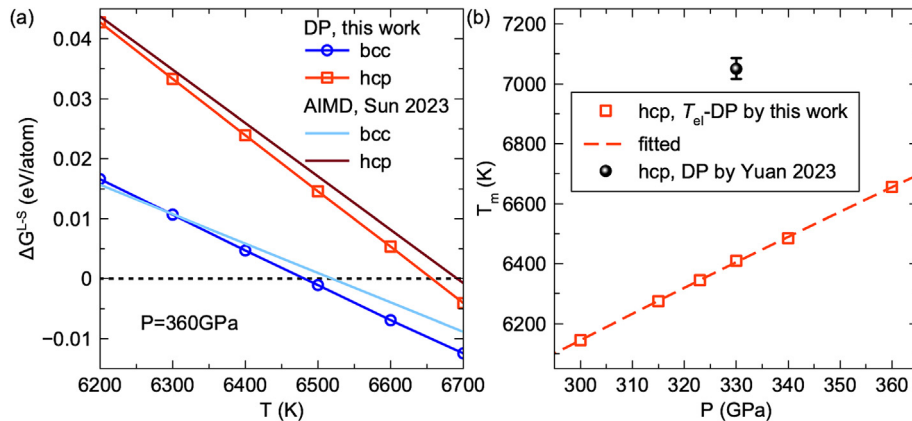


Fig. 4. (a) The Gibbs free energy difference ΔG_{L-S} for bcc and hcp at 360 GPa. The intersection with the dotted line $\Delta G_{L-S} = 0$ defines the melting temperature. The DFT results were from Sun et al. (2023). (b) The melting temperatures of the hcp phase. The data from the present DP model is fitted as $T_m = 3010 + 12.07P - 0.005410P^2$.

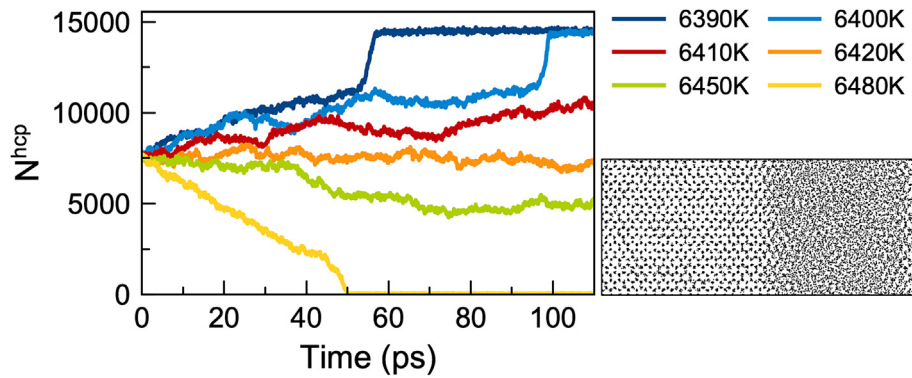


Fig. 5. The melting temperature at 330 GPa from the SLC method. Different curves show the number of hcp atoms as a function of simulation time at different temperatures. The right panel shows a snapshot from the SLC simulation.

lation temperature is below the melting temperature, while the decrease of the hcp atom number indicates the temperature is above the melting temperature. The data in Fig. 5 suggests the melting temperature is ~ 6420 K at 330 GPa. This is consistent with the free energy results of 6410 K at 330 GPa. Therefore, SLC and free energy calculations do not show a significant difference in melting temperature calculations.

3.3. Origin of discrepancy

We have shown that the DP method can accurately describe the EoS and Gibbs free energies for different iron phases under inner core conditions. Unlike Yuan and Steinle-Neumann's (2023) results, the melting temperatures from our DP model are very consistent with the ones from AIMD simulations. In many works, as summarized by Wen et al. (2022), DP models were usually trained on the ground-state, Born-Oppenheimer energy surface, which only considers atomic positions but does not take into account the simulation temperature. Therefore, the effect of electronic entropy was disregarded. This treatment may not be significant for insulating or free-electron-like systems at low temperatures. However, the nature of transition metals leads to strong d-bands close to the Fermi level, causing large electronic entropies in Fe alloys. The high temperature of Earth's core further enhances the

electronic entropy effect, contributing significantly to the energy and pressure of Fe alloy in the core. Therefore, neglecting this term can cause inconsistency in describing the energy of the training datasets collected from different temperatures, as shown in Fig. 2. Because the electronic density of states differs in various Fe phases, the electronic entropy can significantly affect the relative thermodynamic stability of hcp, bcc, and liquid. We believe the disregard for electronic entropy contributed to the underestimation of liquid-free energy in Yuan's DP model, resulting in a high hcp phase melting temperature. We also noticed a few differences in the DFT calculations between ours and Yuan and Steinle-Neumann's (2023) work. We employed the iron's PAW potential with 16 valence electrons ($3s^2 3p^6 3d^6 4s^2$), while Yuan and Steinle-Neumann (2023) used one containing 14 valence electrons ($3p^6 3d^6 4s^2$) without 3s electron contributions. The Brillouin zone was sampled with a $2 \times 2 \times 2$ k-point grid in our DFT calculations, whereas a single Γ point was used in Yuan and Steinle-Neumann's (2023) work. The accumulation of these errors resulted in the significant discrepancy in melting temperature computed from Yuan and Steinle-Neumann (2023). In Fig. 6, we summarize the melting points of the hcp phase at ICB from recent theoretical calculations (Alfè et al., 2002b; Alfè, 2009; Sola and Alfè, 2009; Murphy et al., 2011; Stixrude, 2012; Anzellini et al., 2013; Zhang et al., 2015, 2016; Sun et al., 2018, 2023; Davies et al., 2019; Sinmyo et al.,

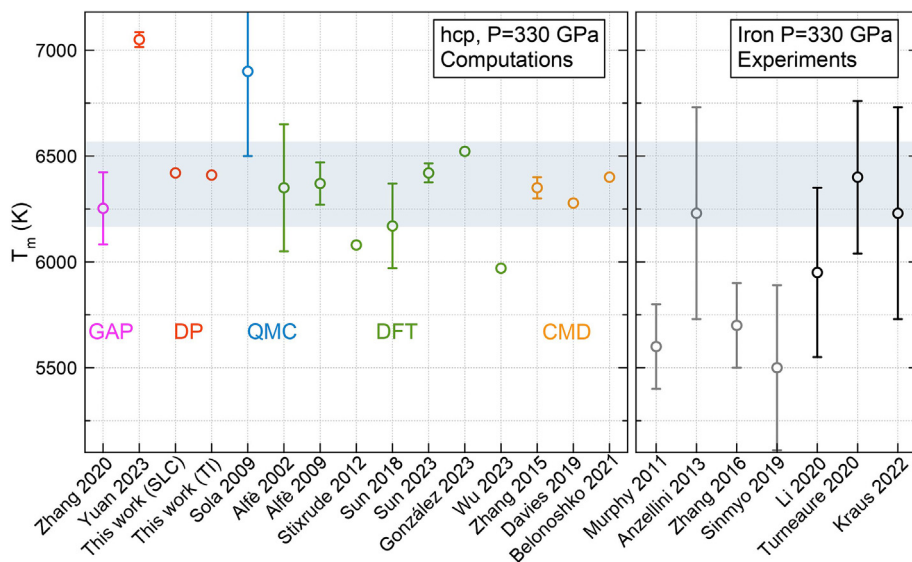


Fig. 6. Current and previous results on hcp iron's melting temperatures obtained from calculations and experiments. The shadow region is 6370 ± 200 K.

2019; Li et al., 2020; Turneure et al., 2020; Belonoshko et al., 2021; Kraus et al., 2022; González-Cataldo and Militzer, 2023; Wu et al., 2023; Yuan and Steinle-Neumann, 2023) and experiments. We find most data are located in the region of 6370 ± 200 K, which can be used as a representative value of iron's melting points at the ICB. In particular, the value is consistent with the latest experimental results reported by Kraus et al. (2022), which suggests a melting temperature of 6230 ± 500 K at 330 GPa. Ni and light elements in the Earth's core can affect the melting behavior of iron (Torchio et al., 2020; Hirose et al., 2021; Oka et al., 2022; Sakai et al., 2023; Sun et al., 2024; Zhang et al., 2023b). The current DP model of pure iron provides a basis to include interactions with other elements by integrating structures of binary or ternary phases into the training dataset in future studies.

4. Conclusion

In summary, we developed an electronic temperature-dependent DP model for iron under inner core conditions. With thermodynamic integration and solid–liquid coexisting methods, we investigate the melting temperature of iron under Earth's inner core conditions. The DP model accurately reproduced energies, forces, and pressures compared to DFT calculations. It provides the EoS and melting temperatures of hcp iron that are consistent with previous AIMD simulations. We resolved the discrepancy of melting temperature from the previous DP model and showed the importance of including electronic entropy effects in describing iron's free energy under inner core conditions. The calculations from the present DP model and most previous computational and experimental data suggest the melting temperature of hcp iron in the region of 6370 ± 200 K at ICB pressure. Our work provides insights into the machine learning melting behavior of iron under core conditions and provides the basis for future development of binary or ternary DP models for iron and other elements in the core.

CRedit authorship contribution statement

Fulun Wu: Writing – review & editing, Writing – original draft, Visualization, Validation, Software, Methodology, Formal analysis, Data curation. **Shunqing Wu:** Writing – review & editing, Supervision, Project administration, Funding acquisition. **Cai-Zhuang Wang:** Writing – review & editing, Software, Formal analysis. **Kai-Ming Ho:** Writing – review & editing, Validation, Methodology, Investigation, Formal analysis. **Renata M. Wentzcovitch:** Writing – review & editing, Supervision, Investigation, Formal analysis. **Yang Sun:** Writing – review & editing, Writing – original draft, Visualization, Validation, Supervision, Software, Resources, Project administration, Methodology, Investigation, Funding acquisition, Formal analysis, Data curation, Conceptualization.

Declaration of competing interest

The authors declare that they have no known competing financial interests or personal relationships that could have appeared to influence the work reported in this paper.

Acknowledgments

Work at Xiamen University was supported by National Natural Science Foundation of China (Grant Nos. 42374108 and 12374015). Y.S. acknowledges support from Fundamental Research Funds for the Central Universities (Grant No. 20720230014). R.M.W. acknowledges support from NSF (Grant Nos. EAR-2000850 and

EAR-1918126). K.M.H. acknowledges support from NSF (Grant No. EAR-1918134). Shaorong Fang and Tianfu Wu from the Information and Network Center of Xiamen University are acknowledged for their help with Graphics Processing Unit (GPU) computing. We acknowledge the supercomputing time supported by the Opening Project of the Joint Laboratory for Planetary Science and Supercomputing (Grant No. CSYGS-QT-2024-15), Research Center for Planetary Science, and the National Supercomputing Center in Chengdu.

Appendix A. Supplementary data

Supplementary data to this article can be found online at <https://doi.org/10.1016/j.gsf.2024.101925>.

References

- Alfè, D., 2009. Temperature of the inner-core boundary of the Earth: melting of iron at high pressure from first-principles coexistence simulations. *Phys. Rev. B* 79, 060101. <https://doi.org/10.1103/PhysRevB.79.060101>.
- Alfè, D., Gillan, M.J., Price, G.D., 2002a. Complementary approaches to the *ab initio* calculation of melting properties. *J. Chem. Phys.* 116, 6170–6177. <https://doi.org/10.1063/1.1460865>.
- Alfè, D., Price, G.D., Gillan, M.J., 2002b. Iron under Earth's core conditions: liquid-state thermodynamics and high-pressure melting curve from *ab initio* calculations. *Phys. Rev. B* 65, 165118. <https://doi.org/10.1103/PhysRevB.65.165118>.
- Anzellini, S., Dewaele, A., Mezouar, M., Loubeyre, P., Morard, G., 2013. Melting of iron at Earth's inner core boundary based on fast X-ray diffraction. *Science* 340, 464–466. <https://doi.org/10.1126/science.1233514>.
- Bartók, A.P., Payne, M.C., Kondor, R., Csányi, G., 2010. Gaussian approximation potentials: the accuracy of quantum mechanics, without the electrons. *Phys. Rev. Lett.* 104, 136403. <https://doi.org/10.1103/PhysRevLett.104.136403>.
- Behler, J., 2021. Four generations of high-dimensional neural network potentials. *Chem. Rev.* 121, 10037–10072. <https://doi.org/10.1021/acs.chemrev.0c00868>.
- Behler, J., Parrinello, M., 2007. Generalized neural-network representation of high-dimensional potential-energy surfaces. *Phys. Rev. Lett.* 98, 146401. <https://doi.org/10.1103/PhysRevLett.98.146401>.
- Belonoshko, A.B., Ahuja, R., Johansson, B., 2000. Quasi-*ab initio* molecular dynamic study of Fe melting. *Phys. Rev. Lett.* 84, 3638–3641. <https://doi.org/10.1103/PhysRevLett.84.3638>.
- Belonoshko, A.B., Fu, J., Smirnov, G., 2022a. Erratum: Free energies of iron phases at high pressure and temperature: Molecular dynamics study [Phys. Rev. B **104**, 104103 (2021)]. *Phys. Rev. B* 105, 059903. <https://doi.org/10.1103/PhysRevB.105.059903>.
- Belonoshko, A.B., Lukinov, T., Fu, J., Zhao, J., Davis, S., Simak, S.I., 2017. Stabilization of body-centred cubic iron under inner-core conditions. *Nat. Geosci.* 10, 312–316. <https://doi.org/10.1038/ngeo2892>.
- Belonoshko, A.B., Fu, J., Smirnov, G., 2021. Free energies of iron phases at high pressure and temperature: molecular dynamics study. *Phys. Rev. B* 104, 104103. <https://doi.org/10.1103/PhysRevB.104.104103>.
- Belonoshko, A.B., Simak, S.I., Olovsson, W., Vekilova, O.Y., 2022. Elastic properties of body-centered cubic iron in Earth's inner core. *Phys. Rev. B* 105, L180102. <https://doi.org/10.1103/PhysRevB.105.L180102>.
- Blöchl, P.E., 1994. Projector augmented-wave method. *Phys. Rev. B* 50, 17953–17979. <https://doi.org/10.1103/PhysRevB.50.17953>.
- Bouchet, J., Mazevet, S., Morard, G., Guyot, F., Musella, R., 2013. *Ab initio* equation of state of iron up to 1500 GPa. *Phys. Rev. B - Condens. Matter Mater. Phys.* 87, 1–8. <https://doi.org/10.1103/PhysRevB.87.094102>.
- Davies, C.J., Pozzo, M., Alfè, D., 2019. Assessing the inner core nucleation paradox with atomic-scale simulations. *Earth Planet. Sci. Lett.* 507, 1–9. <https://doi.org/10.1016/j.epsl.2018.11.019>.
- Deng, J., Niu, H., Hu, J., Chen, M., Stixrude, L., 2023. Melting of MgSiO₃ determined by machine learning potentials. *Phys. Rev. B* 107, 064103. <https://doi.org/10.1103/PhysRevB.107.064103>.
- Deringer, V.L., Bartók, A.P., Bernstein, N., Wilkins, D.M., Ceriotti, M., Csányi, G., 2021. Gaussian process regression for materials and molecules. *Chem. Rev.* 121, 10073–10141. <https://doi.org/10.1021/acs.chemrev.1c00022>.
- Fischer, R.A., 2016. Melting of Fe alloys and the thermal structure of the core. *Geophys. Monogr. Ser.*, 1–12. <https://doi.org/10.1002/9781118992487.ch1>.
- González-Cataldo, F., Militzer, B., 2023. *ab initio* determination of iron melting at terapascal pressures and super-earths core crystallization. *Phys. Rev. Res.* 5, 033194. <https://doi.org/10.1103/PhysRevResearch.5.033194>.
- Gubbins, D., Sreenivasan, B., Mound, J., Rost, S., 2011. Melting of the Earth's inner core. *Nature* 473, 361–363. <https://doi.org/10.1038/nature10068>.
- He, Y., Sun, S., Kim, D.Y., Jang, B.G., Li, H., Mao, H., 2022. Superionic iron alloys and their seismic velocities in Earth's inner core. *Nature* 602, 258–262. <https://doi.org/10.1038/s41586-021-04361-x>.

- Hirose, K., Labrosse, S., Hernlund, J., 2013. Composition and state of the core. *Annu. Rev. Earth Planet. Sci.* 41, 657–691. <https://doi.org/10.1146/annurev-earth-050212-124007>.
- Hirose, K., Wood, B., Vočadlo, L., 2021. Light elements in the Earth's core. *Nat. Rev. Earth Environ.* 2, 645–658. <https://doi.org/10.1038/s43017-021-00203-6>.
- Hou, M., Liu, J., Zhang, Y., Du, X., Dong, H., Yan, L., Wang, J., Wang, L., Chen, B., 2021. Melting of iron explored by electrical resistance jump up to 135 GPa. *Geophys. Res. Lett.* 48, e2021GL095739. <https://doi.org/10.1029/2021GL095739>.
- Jinnouchi, R., Karsai, F., Kresse, G., 2019. On-the-fly machine learning force field generation: application to melting points. *Phys. Rev. B* 100, 014105. <https://doi.org/10.1103/PhysRevB.100.014105>.
- Kingma, D.P., Ba, J., 2014. Adam: a method for stochastic optimization. *ArXiv Prepr. ArXiv1412.6980*. <https://doi.org/10.48550/arXiv.1412.6980>.
- Kohn, W., 1999. Nobel lecture: electronic structure of matter – wave functions and density functional. *Rev. Mod. Phys.* 71, 1253–1266. <https://doi.org/10.1103/revmodphys.71.1253>.
- Kraus, R.G., Hemley, R.J., Ali, S.J., Belof, J.L., Benedict, L.X., Bernier, J., Braun, D., Cohen, R.E., Collins, G.W., Coppari, F., Desjarlais, M.P., Fratanduono, D., Hamel, S., Krygier, A., Lazicki, A., Mcnane, J., Millot, M., Myint, P.C., Newman, M.G., Rygg, J.R., Sterbentz, D.M., Stewart, S.T., Stixrude, L., Swift, D.C., Wehrenberg, C., Eggert, J.H., 2022. Measuring the melting curve of iron at super-Earth core conditions. *Science* 375, 202–205. <https://doi.org/10.1126/science.abm1472>.
- Kresse, G., Furthmüller, J., 1996. Efficient iterative schemes for *ab initio* total-energy calculations using a plane-wave basis set. *Phys. Rev. B* 54, 11169–11186. <https://doi.org/10.1103/PhysRevB.54.11169>.
- Kresse, G., Hafner, J., 1993. *ab initio* molecular dynamics for liquid metals. *Phys. Rev. B* 47, 558–561. <https://doi.org/10.1103/PhysRevB.47.558>.
- Kuwayama, Y., Morard, G., Nakajima, Y., Hirose, K., Baron, A.Q.R., Kawaguchi, S.I., Tsuchiya, T., Ishikawa, D., Hirao, N., Ohishi, Y., 2020. Equation of state of liquid iron under extreme conditions. *Phys. Rev. Lett.* 124, 165701. <https://doi.org/10.1103/PhysRevLett.124.165701>.
- Laio, A., Bernard, S., Chiarotti, G.L., Scandolo, S., Tosatti, E., 2000. Physics of iron at Earth's core conditions. *Science* 287, 1027–1030. <https://doi.org/10.1126/science.287.5455.1027>.
- Larsen, P.M., Schmidt, S., Schiøtz, J., 2016. Robust structural identification via polyhedral template matching. *Model. Simul. Mater. Sci. Eng.* 24, 055007. <https://doi.org/10.1088/0965-0393/24/5/055007>.
- Li, J., Wu, Q., Li, J., Xue, T., Tan, Y., Zhou, X., Zhang, Y., Xiong, Z., Gao, Z., Sekine, T., 2020. Shock melting curve of iron: a consensus on the temperature at the Earth's inner core boundary. *Geophys. Res. Lett.* 47, e2020GL087758. <https://doi.org/10.1029/2020GL087758>.
- Liu, J., Sun, Y., Lv, C., Zhang, F., Fu, S., Prapapenka, V.B., Wang, C., Ho, K., Lin, J., Wentzcovitch, R.M., 2023. Iron-rich Fe-O compounds at Earth's core pressures. *The Innovation* 4 (1), 100354. <https://doi.org/10.1016/j.xinn.2022.100354>.
- Luo, H., Karki, B.B., Ghosh, D.B., Bao, H., 2021. Anomalous behavior of viscosity and electrical conductivity of MgSiO₃ melt at mantle conditions. *Geophys. Res. Lett.* 48, e2021GL093573. <https://doi.org/10.1029/2021GL093573>.
- Luo, C., Sun, Y., Wentzcovitch, R.M., 2024. Probing the state of hydrogen in δ -AlOOH at mantle conditions with machine learning potential. *Phys. Rev. Res.* 6, 013292. <https://doi.org/10.1103/PhysRevResearch.6.013292>.
- Martorell, B., Brodholt, J., Wood, I.G., Vočadlo, L., 2015. The elastic properties and stability of fcc-Fe and fcc-FeNi alloys at inner-core conditions. *Geophys. J. Int.* 202, 94–101. <https://doi.org/10.1093/gji/ggv128>.
- Mermin, N.D., 1965. Thermal properties of the inhomogeneous electron gas. *Phys. Rev.* 137, A1441–A1443. <https://doi.org/10.1103/PhysRev.137.A1441>.
- Morris, J.R., Wang, C.Z., Ho, K.M., Chan, C.T., 1994. Melting line of aluminum from simulations of coexisting phases. *Phys. Rev. B* 49, 3109–3115. <https://doi.org/10.1103/PhysRevB.49.3109>.
- Murphy, C.A., Jackson, J.M., Sturhahn, W., Chen, B., 2011. Melting and thermal pressure of hcp-Fe from the phonon density of states. *Phys. Earth Planet. Inter.* 188, 114–120. <https://doi.org/10.1016/j.pepi.2011.07.001>.
- Nimmo, F., 2015. Energetics of the core. In: Schubert, G. (Ed.), *Treatise on Geophysics*. Elsevier, pp. 27–55. <https://doi.org/10.1016/B978-0-444-53802-4.00139-1>.
- Oka, K., Ikuta, N., Tagawa, S., Hirose, K., Ohishi, Y., 2022. Melting experiments on Fe-O-H and Fe-H: evidence for eutectic melting in Fe-FeH and implications for hydrogen in the core. *Geophys. Res. Lett.* 49, e2022GL099420. <https://doi.org/10.1029/2022GL099420>.
- Perdew, J.P., Burke, K., Ernzerhof, M., 1996. Generalized gradient approximation made simple. *Phys. Rev. Lett.* 77, 3865–3868. <https://doi.org/10.1103/PhysRevLett.77.3865>.
- Sakai, F., Hirose, K., Morard, G., 2023. Partitioning of silicon and sulfur between solid and liquid iron under core pressures: constraints on Earth's core composition. *Earth Planet. Sci. Lett.* 624, 118449. <https://doi.org/10.1016/j.epsl.2023.118449>.
- Sinmyo, R., Hirose, K., Ohishi, Y., 2019. Melting curve of iron to 290 GPa determined in a resistance-heated diamond-anvil cell. *Earth Planet. Sci. Lett.* 510, 45–52. <https://doi.org/10.1016/j.epsl.2019.01.006>.
- Sola, E., Alfè, D., 2009. Melting of iron under Earth's core conditions from diffusion monte carlo free energy calculations. *Phys. Rev. Lett.* 103, 078501. <https://doi.org/10.1103/PhysRevLett.103.078501>.
- Steinle-Neumann, G., Stixrude, L., Cohen, R.E., Gülseren, O., 2001. Elasticity of iron at the temperature of the Earth's inner core. *Nature* 413, 57–60. <https://doi.org/10.1038/35092536>.
- Stixrude, L., 2012. Structure of Iron to 1 Gbar and 40 000 K. *Phys. Rev. Lett.* 108, 055505. <https://doi.org/10.1103/PhysRevLett.108.055505>.
- Sun, T., Brodholt, J.P., Li, Y., Vočadlo, L., 2018. Melting properties from *ab initio* free energy calculations: iron at the Earth's inner-core boundary. *Phys. Rev. B* 98, 224301. <https://doi.org/10.1103/PhysRevB.98.224301>.
- Sun, Y., Zhang, F., Ye, Z., Zhang, Y., Fang, X., Ding, Z., Wang, C.-Z., Mendelev, M.I., Ott, R.T., Kramer, M.J., Ho, K.-M., 2016. 'Crystal Genes' in metallic liquids and glasses. *Sci. Rep.* 6, 23734. <https://doi.org/10.1038/srep23734>.
- Sun, Y., Zhang, F., Mendelev, M.I., Wentzcovitch, R.M., Ho, K.-M., 2022. Two-step nucleation of the Earth's inner core. *Proc. Natl. Acad. Sci.* 119, e2113059119. <https://doi.org/10.1073/pnas.2113059119>.
- Sun, Y., Mendelev, M.I., Zhang, F., Liu, X., Da, B., Wang, C., Wentzcovitch, R.M., Ho, K., 2023. *Ab initio* melting temperatures of bcc and hcp iron under the Earth's inner core condition. *Geophys. Res. Lett.* 50, e2022GL102447. <https://doi.org/10.1029/2022GL102447>.
- Sun, Y., Mendelev, M.I., Zhang, F., Liu, X., Da, B., Wang, C.-Z., Wentzcovitch, R.M., Ho, K.-M., 2024. Unveiling the effect of Ni on the formation and structure of Earth's inner core. *Proc. Natl. Acad. Sci.* 121, e2316477121. <https://doi.org/10.1073/pnas.2316477121>.
- Tang, L., Zhang, C., Sun, Y., Ho, K.-M., Wentzcovitch, R.M., Wang, C.-Z., 2023. Structure and dynamics of Fe₉₀Si₁₀O₇ liquids close to Earth's liquid core conditions. *Phys. Rev. B* 108, 064104. <https://doi.org/10.1103/PhysRevB.108.064104>.
- Torchio, R., Boccato, S., Miozzi, F., Rosa, A.D., Ishimatsu, N., Kantor, I., Sévelin-Radiguet, N., Briggs, R., Meneghini, C., Irfune, T., Morard, G., 2020. Melting curve and phase relations of Fe-Ni Alloys: implications for the Earth's core composition. *Geophys. Res. Lett.* 47, e2020GL088169. <https://doi.org/10.1029/2020GL088169>.
- Turneare, S.J., Sharma, S.M., Gupta, Y.M., 2020. Crystal structure and melting of Fe shock compressed to 273 GPa: *in situ* X-ray diffraction. *Phys. Rev. Lett.* 125, 215702. <https://doi.org/10.1103/PhysRevLett.125.215702>.
- Unke, O.T., Chmiela, S., Sauceda, H.E., Gastegger, M., Poltavsky, I., Schütt, K.T., Tkatchenko, A., Müller, K.-R., 2021. Machine learning force fields. *Chem. Rev.* 121, 10142–10186. <https://doi.org/10.1021/acs.chemrev.0c01111>.
- Vočadlo, L., Wood, I.G., Gillan, M.J., Brodholt, J., Dobson, D.P., Price, G.D., Alfè, D., 2008. The stability of bcc-Fe at high pressures and temperatures with respect to tetragonal strain. *Phys. Earth Planet. Inter.* 170, 52–59. <https://doi.org/10.1016/j.pepi.2008.07.032>.
- Voosen, P., 2022. The planet inside. *Science* 376, 18–22. <https://doi.org/10.1126/science.abq2090>.
- Wan, T., Luo, C., Sun, Y., Wentzcovitch, R.M., 2024. Thermoelastic properties of bridgmanite using deep-potential molecular dynamics. *Phys. Rev. B* 109, 094101. <https://doi.org/10.1103/PhysRevB.109.094101>.
- Wen, T., Zhang, L., Wang, H., E, W., Srolovitz, D.J., 2022. Deep potentials for materials science. *Mater. Futur.* 1, 022601. <https://doi.org/10.1088/2752-5724/ac681d>.
- Wen, T.Q., Tang, L., Sun, Y., Ho, K.M., Wang, C.Z., Wang, N., 2017. Crystal genes in a marginal glass-forming system of Ni₅₀Zr₅₀. *Phys. Chem. Chem. Phys.* 19, 30429–30438. <https://doi.org/10.1039/C7CP05976K>.
- Wentzcovitch, R.M., Martins, J.L., Allen, P.B., 1992. Energy versus free-energy conservation in first-principles molecular dynamics. *Phys. Rev. B* 45, 11372–11374. <https://doi.org/10.1103/PhysRevB.45.11372>.
- Wilson, A.J., Alfè, D., Walker, A.M., Davies, C.J., 2023. Can homogeneous nucleation resolve the inner core nucleation paradox? *Earth Planet. Sci. Lett.* 614, 118176. <https://doi.org/10.1016/j.epsl.2023.118176>.
- Wu, Z., Wang, W., 2022. Shear softening of earth's inner core as indicated by its high poisson ratio and elastic anisotropy. *Fundam. Res.* <https://doi.org/10.1016/j.fmr.2022.08.010>.
- Wu, C.J., Benedict, L.X., Myint, P.C., Hamel, S., Prisbrey, C.J., Leek, J.R., 2023. Wide-ranged multiphase equation of state for iron and model variations addressing uncertainties in high-pressure melting. *Phys. Rev. B* 108, 014102. <https://doi.org/10.1103/PhysRevB.108.014102>.
- Wu, F., Sun, Y., Wan, T., Wu, S., Wentzcovitch, R.M., 2024. Deep-learning-based prediction of the tetragonal → cubic transition in davemaoite. *Geophys. Res. Lett.* 51, e2023GL108012. <https://doi.org/10.1029/2023GL108012>.
- Yang, F., Zeng, Q., Chen, B., Kang, D., Zhang, S., Wu, J., Yu, X., Dai, J., 2022. Lattice thermal conductivity of MgSiO₃ perovskite and post-perovskite under lower mantle conditions calculated by deep potential molecular dynamics. *Chin. Phys. Lett.* 39, 116301. <https://doi.org/10.1088/0256-307X/39/11/116301>.
- Yuan, L., Steinle-Neumann, G., 2023. Hydrogen distribution between the Earth's inner and outer core. *Earth Planet. Sci. Lett.* 609, 118084. <https://doi.org/10.1016/j.epsl.2023.118084>.
- Yuan, L., 2023. Yuan & Steinle-Neumann Training dataset. <https://doi.org/10.6084/M9.FIGSHARE.19773109.V4>.
- Zhang, Z., Csányi, G., Alfè, D., 2020b. Partitioning of sulfur between solid and liquid iron under Earth's core conditions: constraints from atomistic simulations with machine learning potentials. *Geochim. Cosmochim. Acta* 291, 5–18. <https://doi.org/10.1016/j.gca.2020.03.028>.
- Zhang, L., Han, J., Wang, H., Car, R., E, W., 2018a. Deep potential molecular dynamics: a scalable model with the accuracy of quantum mechanics. *Phys. Rev. Lett.* 120, 143001. <https://doi.org/10.1103/PhysRevLett.120.143001>.
- Zhang, L., Han, J., Wang, H., Saidi, W.A., Car, R., E, W., 2018b. End-to-end symmetry preserving inter-atomic potential energy model for finite and extended systems. <https://doi.org/10.48550/arXiv.1805.09003>.
- Zhang, Y.Z., Gao, C., Liu, Q.R., Zhang, L.F., Wang, H., Chen, M.H., 2020a. Warm dense matter simulation via electron temperature dependent deep potential molecular dynamics. *Phys. Plasmas* 27. <https://doi.org/10.1063/5.0023265>.

- Zhang, D., Jackson, J.M., Zhao, J., Sturhahn, W., Alp, E.E., Hu, M.Y., Toellner, T.S., Murphy, C.A., Prakapenka, V.B., 2016. Temperature of Earth's core constrained from melting of Fe and Fe_{0.9}Ni_{0.1} at high pressures. *Earth Planet. Sci. Lett.* 447, 72–83. <https://doi.org/10.1016/j.epsl.2016.04.026>.
- Zhang, Y., Lin, J.-F., 2022. Molten iron in Earth-like exoplanet cores. *Science* 375, 146–147. <https://doi.org/10.1126/science.abn2051>.
- Zhang, W.-J., Liu, Z.-Y., Liu, Z.-L., Cai, L.-C., 2015. Melting curves and entropy of melting of iron under Earth's core conditions. *Phys. Earth Planet. Inter.* 244, 69–77. <https://doi.org/10.1016/j.pepi.2014.10.011>.
- Zhang, Z., Sun, Y., Wentzcovitch, R.M., 2023b. PBE-GGA predicts the B8↔B2 phase boundary of FeO at Earth's core conditions. *Proc. Natl. Acad. Sci.* 120, e2304726120. <https://doi.org/10.1073/pnas.2304726120>.
- Zhang, C., Tang, L., Sun, Y., Ho, K.-M., Wentzcovitch, R.M., Wang, C.-Z., 2022. Deep machine learning potential for atomistic simulation of Fe-Si-O systems under Earth's outer core conditions. *Phys. Rev. Mater.* 6, 063802. <https://doi.org/10.1103/PhysRevMaterials.6.063802>.
- Zhang, Y., Wang, Y., Huang, Y., Wang, J., Liang, Z., Hao, L., Gao, Z., Li, J., Wu, Q., Zhang, H., Liu, Y., Sun, J., Lin, J.-F., 2023a. Collective motion in hcp-Fe at Earth's inner core conditions. *Proc. Natl. Acad. Sci.* 120, e2309952120. <https://doi.org/10.1073/pnas.2309952120>.
- Zhuang, J., Wang, H., Zhang, Q., Wentzcovitch, R.M., 2021. Thermodynamic properties of ϵ -Fe with thermal electronic excitation effects on vibrational spectra. *Phys. Rev. B* 103, 144102. <https://doi.org/10.1103/PhysRevB.103.144102>.